Electrical Characterization and Transmission Electron Microscopy Assessment of Isolation of AlGaN/GaN High Electron Mobility Transistors with Oxygen Ion Implantation

2010 Jpn. J. Appl. Phys. 49 021001

(http://iopscience.iop.org/1347-4065/49/2R/021001)

Electrical Characterization and Transmission Electron Microscopy Assessment of Isolation of AlGaN/GaN High Electron Mobility Transistors with Oxygen Ion Implantation

Jin-Yu Shiu, Chung-Yu Lu, Ting-Yi Su[2], Rong-Tan Huang[3], Herbert Zirath[1], Niklas Rorsman[1], and Edward Yi Chang*

Department of Materials Science and Engineering, National Chiao Tung University, Hsinchu 300, Taiwan, R.O.C.
[1]*Microwave Electronics Laboratory, Microtechnology and Nanoscience Chalmers University of Technology, SE 412 96 Gothenburg, Sweden*
[2]*Department of Engineering and System Science, National Tsing Hua University, Hsinchu 300, Taiwan, R.O.C.*
[3]*Institute of Materials Engineering, National Taiwan Ocean University, Keelung 202-24, Taiwan, R.O.C.*

Received April 19, 2009; revised August 6, 2009; accepted August 27, 2009; published online February 22, 2010

A multienergy oxygen ion implantation process was demonstrated to be compatible with the processing of high-power microwave AlGaN/GaN high electron mobility transistors (HEMTs). A high sheet resistivity and thermally stable isolation were demonstrated. The microstructures of implanted and postannealed specimens were investigated by transmission electron microscopy (TEM). The dependences of the sheet resistivity and different postannealing temperatures were correlated with the defect clusters and microstructure of lattice stacking faults. After 300 °C annealing, the sheet resistivity was higher than 10^{12} Ω/square, which was attributed to the severe defect interaction eliminating the trapping centers and reducing the leakage current. A maximum output power density of 5.3 W/mm at $V_{gs} = -4$ V and $V_{ds} = 50$ V at 3 GHz was demonstrated on lag-free HEMTs without field plates on sapphire substrate.

DOI: 10.1143/JJAP.49.021001

1. Introduction

GaN based high electron mobility transistors (HEMTs) have attracted considerable attention owing to their excellent performance for microwave, high-power, and high-temperature applications. AlGaN/GaN HEMTs have shown much higher output power density at microwave frequencies than GaAs- or Si-based transistors. Device isolation of GaN-based HEMTs is conventionally realized by dry etching to define the device active region.[1)] However, implantation isolation has the advantage in the sense that it maintains the planarity of the device, which increases the yield and uniformity of GaN HEMT and monolithic microwave integrated circuit (MMIC) processes.

Implantation isolation has been studied in pure GaN or AlGaN materials using H^+, He^+, N^+, F^+, Mg^+, Ar^+, and Zn^+ ions.[2–8)] The O^+ ion implantation isolation was also investigated on AlGaAs,[9)] InAlN,[10)] and GaN (n-type doping)/GaN materials,[11)] to study the isolation quality and P/He, Ar^+, and N^+ ion implantations have been carried out in the isolation of AlGaN/GaN HEMTs.[12–14)]

In this study, multienergy O^+ ion implantation was applied for isolation in the fabrication of AlGaN/GaN HEMTs. The motivations for this are as follows. Firstly, O^+ ion implantation isolation has better thermal stability than light atomic mass ion (i.e., H^+ or He^+). Secondly, the lower implantation incident energy decreases the probability of surface damage of the device and increases the yield. Thirdly, multiple incident energy and higher implantation ion density were used to ensure high quality isolation in both AlGaN Schottky and GaN buffer layers with a good thermal stability. The latter motivations are important in the discussion of isolation processes for full HEMT device processes,[15)] as compared with isolation tests.

Two major mechanisms concerning oxygen implantation isolation used for GaN-based HEMT isolation need to be confirmed, especially after the thermal annealing treatment. Firstly, is the isolation mechanism a physical damage or chemical compensation? Secondly, the TRIM calculation of atomic displacement only accounts for the ballistic process and neglects dynamic annealing (i.e., defect interaction process). However, ion-generated point defects that survive after the quenching of collision cascades may migrate through the lattice and experience annihilation and cluster formation.[16)] For real GaN HEMT application, the post thermal annealing phenomenon should be considered because of subsequent high-temperature processes [300 °C plasma-enhanced chemical vapor deposition (PECVD) passivation] and the operational channel temperature of AlGaN/GaN power HEMTs, which may be above 300 °C.[17)]

In this paper, we focus on the analysis of an in-house O^+ implantation process with different postannealing temperatures (T_as).[15)] The effects of the ambient temperature and time on the sheet resistivity were investigated. Tunneling electron microscopy (TEM) analysis was carried out to understand the phenomena in the implanted area after annealing at different temperatures. Finally, the high-performance results of AlGaN/GaN HEMTs using the ion implantation process were demonstrated.

2. Experimental Methods

AlGaN/GaN heterostructures were grown on sapphire by metal–organic chemical vapor deposition (MOCVD) by Hitachi Cable Corporation. They consist of a 2-μm-thick unintentionally doped GaN buffer layer followed by 30-nm-thick undoped $Al_{0.3}Ga_{0.7}N$ Schottky layer. From Hall measurements, the sheet carrier concentration and electron mobility were determined to be 1×10^{13} cm^{-2} and 900 cm^2/(V·s), respectively.

The TRIM software was used to simulate the implantation process.[2)] Figure 1 shows the simulated depth profile of the distribution of the implanted O^+ ions, and damage vacancies created by the implantation. The lower ion concentration near the wafer surface, below 50 nm [Fig. 1(a)], is of concern in the AlGaN/GaN HEMT process. Nevertheless, Fig. 1(b) shows a different shape vacancy depth profile without the surface low vacancy concentration problem.

The HEMT devices were $2 \times 50 \times 0.6$ μm^2 gates defined in the middle of the 4 μm source-drain spacing. The epiwafers were first cleaned using a standard degreasing procedure and a standard RCA clean. Ohmic contacts were formed by e-beam evaporation of a Ti/Al/Ni/Au multilayer

*E-mail address: edc@mail.nctu.edu.tw

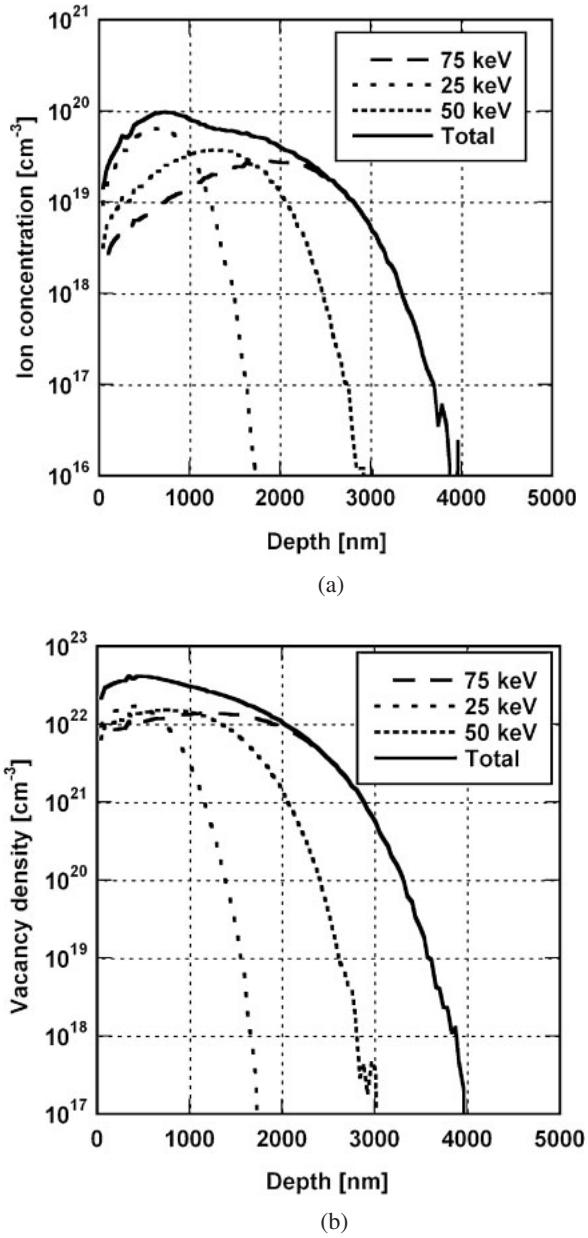

Fig. 1. Depth profile of the distribution of (a) implanted O^+ ions and (b) damaged vacancy created from the implantation. Estimated with the TRIM software.

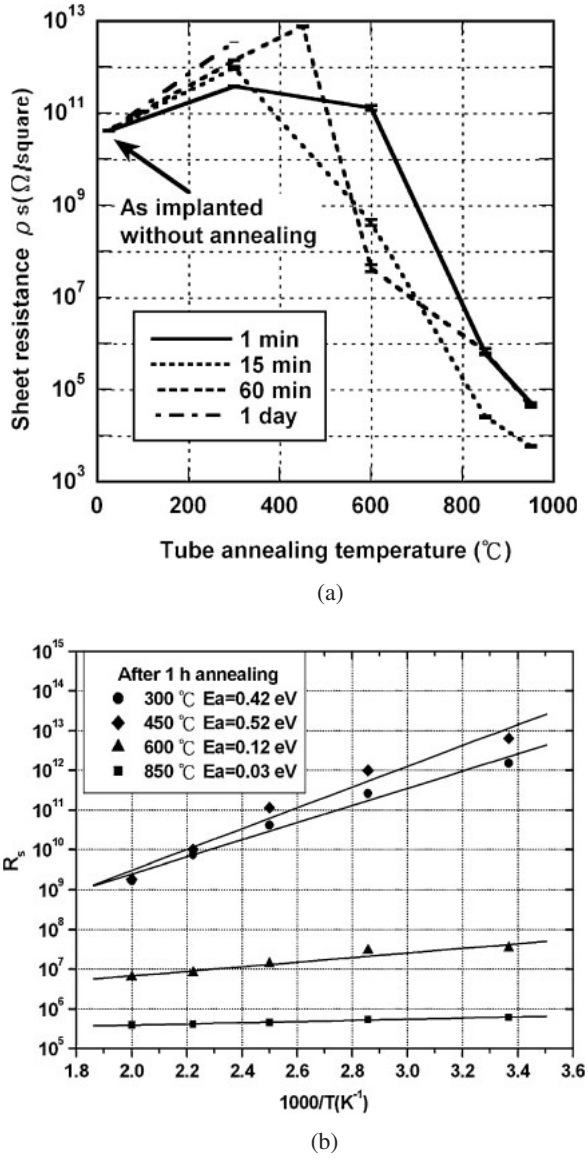

Fig. 2. (a) Sheet resistivity vs annealing temperature with different annealing times. (b) Arrhenius plot showing activation energy (E_a) calculated from linear fitting curve of sheet resistivity with different annealing temperatures.

followed by rapid thermal annealing (RTA) in a nitrogen environment at 850 °C for 30 s. The ohmic contact process step was done prior to the implantation isolation process. A typical contact resistance of 0.2 Ω·mm was measured on chip using TLM patterns. For the transistor process, the photoresist S1818 was used as an implantation mask to define the active region of the isolation testing sample and devices. All the samples were subjected to O^+ ion implantation with implantation energies of 25, 50, and 75 keV, and the dose is 5×10^{14} cm^{-2} for each energy. The 0.6-μm-long gates were defined by electron beam lithography, and the Ni/Au gate metallization was deposited by e-beam evaporation. The transistors were passivated using SiN_x by PECVD at 300 °C, followed by the etching of probing windows using a fluorine-based RIE process.[18)]

The isolation test structure used in this work consisted of two 100-μm-wide ohmic contacts with a separation of 5 μm. On these samples, the implantation process was carried out after the ohmic contact process without any active region definition.

Atomic force microscopy (AFM) analysis was utilized after implantation and post high temperature process to investigate the surface morphology. The TEM specimens were prepared by manual lapping before fine polishing by Ar-ion milling (Gatan precision ion polishing system). The TEM investigation was performed using the JEOL JEM-2010F FEG.

3. Results and Discussion

3.1 Resistivity testing

The sheet resistivity (ρ_{sh}) vs ambient temperature (T_a) was measured on the isolation test structures after different annealing times [Fig. 2(a)]. ρ_{sh} is higher than 10^{12} Ω/square up to at least 450 °C annealing. After 100 h of annealing at 300 °C, the implanted material ρ_{sh} was 4.3×10^{12} Ω/square, which is higher than that of the sample with 1 h of annealing.

The thermal stability of the O^+ implantation is hence appropriate for subsequent HEMT processes (i.e., CVD SiN_x passivation at 300 °C) and normal operation.[17)]

ρ_{sh} initially increases with T_a and goes through a maximum at 450 °C for all postannealing experiments. Pearton *et al.* explained this phenomenon as follows. The density of implant-induced damage sites is reduced and the probability for the trapped electrons to hop from one site to another (resistive (ohmic) current) decreases, until the hopping conduction reaches a minimum.[19)] The Poole–Frenkel effect is another damage-induced mechanism described in the literature.[8,20)] The field-enhanced thermal excitation of trapped electrons would get into the conduction band and increase the leakage current. This effect is also a function of the density of the trapping centers.[20)] Pearton *et al.* claimed that the stable high ρ_{sh} after high-temperature annealing can be explained on the basis of the chemical compensation of the electrons by deep O-related acceptors like in the AlGaAs material.[11,19)] By relying on those investigations, the variation of ρ_{sh} with different T_as in our case can be completely explained on the basis of the damage-induced compensation. We use TEM analysis to investigate the physical damage-induced phenomenon in the specimens after annealing with our optimized HEMT implantation isolation process.[15)]

The sheet resistances of these samples were also measured as a function of temperature, and a temperature-activated behavior was observed. From this, we obtained activation energies of 0.43, 0.52, 0.12, and 0.03 eV at 300, 450, 600, and 850 °C, respectively [Fig. 2(b)].

3.2 Material analysis

The rms of surface morphology on our wafers before implantation is 0.44 nm. The AFM analysis (Fig. 3) shows very good surface morphology after implantation and even after 1 h of high temperature (950 °C) postannealing. This is important to achieve good yield and uniformity in GaN HEMT and MMIC processes.

Figure 4 shows cross-sectional bright-field TEM (XTEM) images after 1 h of annealing at different T_as. Some defect clusters are observed in the implanted region of the as-implanted sample, especially close to the AlGaN-GaN interface [Fig. 4(a)]. However, much clearer defect clusters can be noted on the sample postannealed at 300 °C [Fig. 4(b)]. With higher T_a, a gradual annihilation of the defect clusters is observed [Figs. 4(c) and 4(d)]. These results indicate that the dependence of ρ_{sh} correlates with the defect clusters.

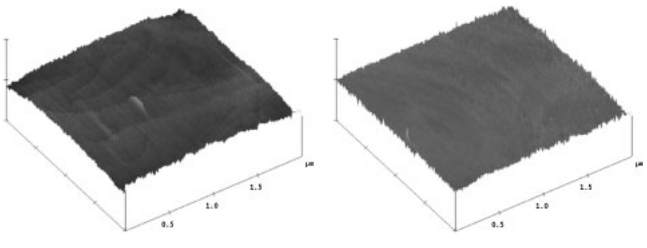

(a) (b)

Fig. 3. AFM surface morphology analysis after implantation, the scan area is 4 μm^2. (a) Without thermal annealing, the wafer showed R_{rms} of 0.34 nm. (b) After 950 °C and 1 h of postannealing, the wafer showed R_{rms} of 0.35 nm.

These results provide evidence that the dynamic annealing during the implantation and the postannealing (subsequent SiN_x passivation and device channel self-heating under operation) affect the defect interaction process. This type of defect cluster formation could change with different T_as affecting the implant-induced point defects interaction. More obvious defect clusters display a severe defect interaction and reduce the density of point defect sites, and the probability for the trapped electrons to hop from one site to another (resistive current) and to be excited into the conduction band (Poole–Frenkel effect) decreases.[8,19,20)] The results also indicate that this type of implantation is suitable for AlGaN/GaN HEMTs that have operation channel temperatures of at least up to 300 °C.[17)]

3.3 Device performance

HEMTs with $2 \times 50 \times 0.6\,\mu m^2$ gates defined in the middle of the 4 μm source-drain spacing were processed on the same AlGaN/GaN structure grown on a sapphire substrate. Comparing the DC and pulsed current–voltage (I–V) characteristics of the HEMTs, with short 100 ns pulse time and 0.1% duty cycle, is an effective way to clarify the gate-lag and drain-lag effects at the same time.[21,22)] Figure 5 shows three different measurements: DC, pulsed from $V_{gs} = 0$ V, $V_{ds} = 0$ V (pulsed #1), and pulsed from $V_{gs} = V_{pinch}$, $V_{ds} = 20$ V (mimicking a class B operation, pulsed #2).[22)] The pulsed #1 measurement shows a higher current than DC owing to the absence of a self-heating effect. The pulsed #2 measurement shows almost no current collapse. On the basis of DC, and pulsed I–V measurements, we conclude that the O^+ ion implantation isolation does not introduce trapping problems. The extrinsic cut-off frequency (f_T) and maximum oscillation frequency (f_{max}) calculated from s-parameters measured up to 50 GHz VNA were 33 and 57 GHz, respectively. The large signal performance of the devices was determined by CW load–pull measurements at 3 GHz without active cooling. The saturated output power density is 4.5 W/mm with 51.5% power added efficiency (PAE) at $V_{ds} = 30$ V, $V_{gs} = -4$ V. The highest output power density was 5.3 W/mm at $V_{ds} = 50$ V, $V_{gs} = -4$ V (Fig. 6).[15)]

4. Conclusions

The multienergy oxygen ion implantation process was investigated by Monte Carlo computer simulation (TRIM), sheet resistivity and thermal stability isolation test, material analysis (AFM, TEM), and AlGaN/GaN HEMT demonstration. There is a clear correlation between the sheet resistivity (after different T_as) and TEM analysis results. From XTEM investigation results, the defect cluster formation changed with different T_as affecting the ion generated point defects interaction. Fewer implant-induced point defects reduce the probability of trapped electrons to hop from one site to another and to be excited to the conduction band. Finally, the devices were processed and characterized to demonstrate the compability of the multi-energy oxygen ion implantation process in dispersion-free high-frequency and high-power AlGaN/GaN HEMT processing and operation.

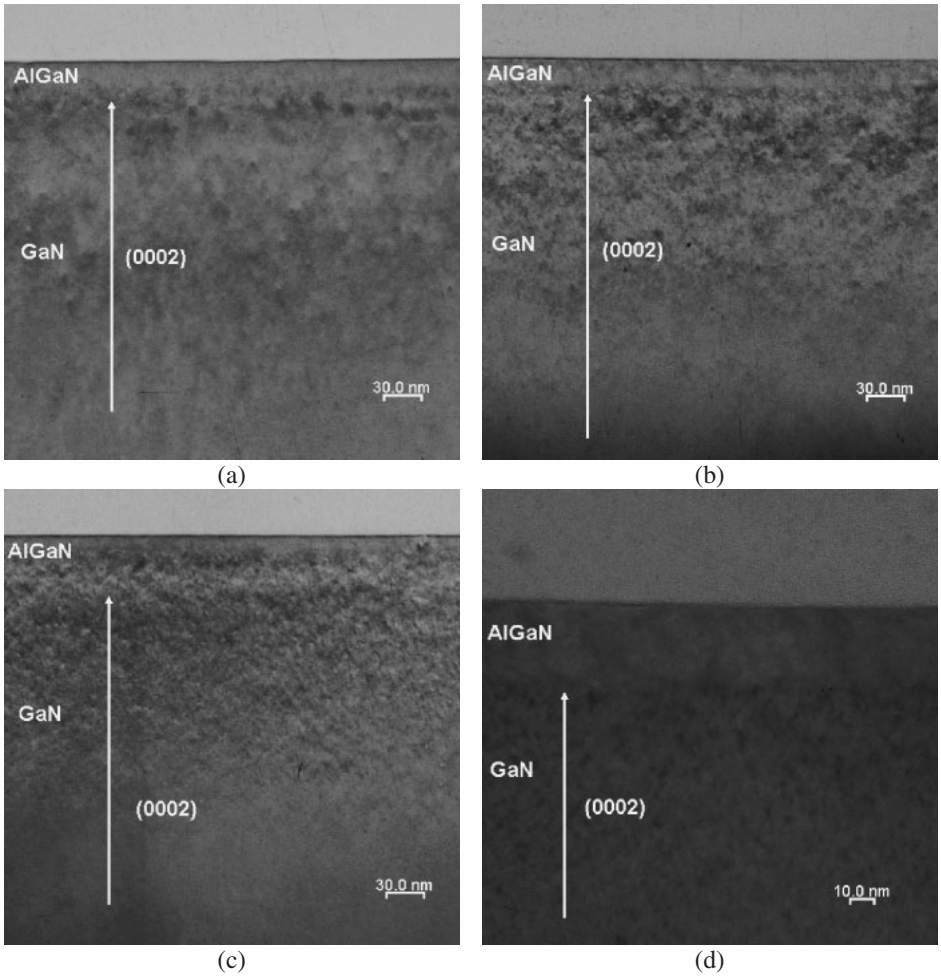

Fig. 4. Cross-sectional bright-field TEM images of (a) as-implanted without annealing, (b) after 300 °C, (c) after 600 °C, and (d) after 850 °C postannealing for 1 h.

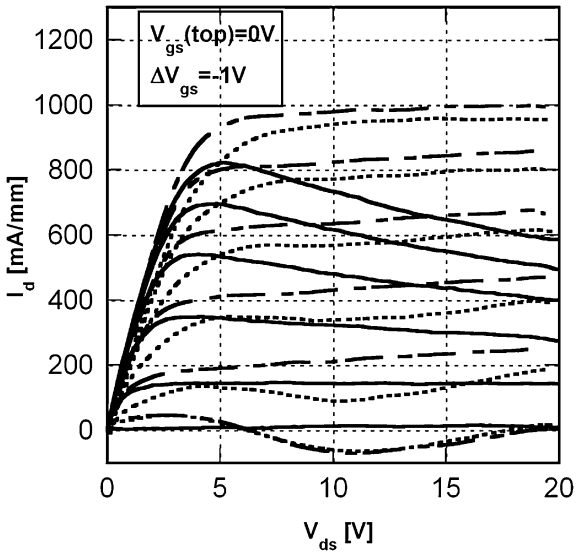

Fig. 5. Pulsed *I*–*V* characteristics of O^+-implanted HEMT under different quiescent states (V_{gs}, V_{ds}) (0 V, 0 V) (dashed line), (V_{pinch}, 20 V) (dotted line), and DC (solid line).

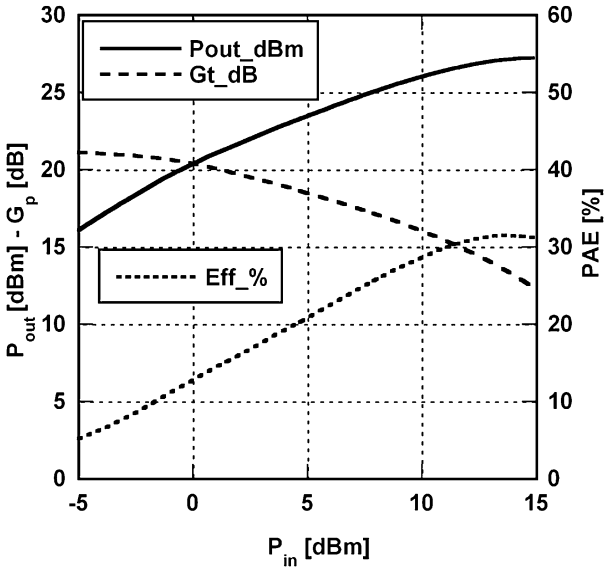

Fig. 6. Power sweep at $V_{ds} = 50$ V, $V_{gs} = -4$ V, showing 5.3 W/mm saturated output power density.

Acknowledgements

The authors at NCTU would like to acknowledge the Ministry of Education, the Ministry of Economic Affairs, and the National Science Council of the Republic of China for supporting this research under the contracts NSC 94-2752-E-009-001-PAE and 94-EC-17-A-05-S1-020. We also thank the Hitachi Cable Corp. for providing the high-quality wafer and NTHU Nuclear Science and Technology Development Center/Instrument Division for carrying out stable implantation.

1) U. K. Mishra, P. Parikh, and Y. F. Wu: Proc. IEEE **90** (2002) 1022.
2) S. C. Binari, H. B. Dietrich, G. Kelner, L. B. Rowland, K. J. Doverspike, and D. K. Wickenden: J. Appl. Phys. **78** (1995) 3008.
3) S. J. Pearton, C. B. Vartuli, J. C. Zolper, C. Yuan, and R. A. Stall: Appl. Phys. Lett. **67** (1995) 1435.
4) R. G. Wilson, C. B. Vartuli, C. R. Abernathy, S. J. Pearton, and J. M. Zavada: Solid-State Electron. **38** (1995) 1329.
5) J. C. Zolper: J. Cryst. Growth **178** (1997) 157.
6) B. Boudart, Y. Guhel, J. C. Pesant, P. Dhamelincourt, and M. A. Poisson: J. Raman Spectrosc. **33** (2002) 283.
7) B. Boudart, Y. Guhel, J. C. Pesant, P. Dhamelincourt, and M. A. Poisson: J. Phys.: Condens. Matter **16** (2004) S49.
8) T. Oishi, N. Miura, M. Suita, T. Nanjo, Y. Abe, T. Ozeki, H. Ishikawa, T. Egawa, and T. Jimbo: J. Appl. Phys. **94** (2003) 1662.
9) J. C. Zolper, A. G. Baca, and S. A. Chalmers: Appl. Phys. Lett. **62** (1993) 2536.
10) S. J. Pearton, J. C. Zolper, R. J. Shul, and F. Ren: J. Appl. Phys. **94** (2003) 1662.
11) G. Dang, X. A. Cao, F. Ren, S. J. Pearton, J. Han, A. G. Baca, and R. J. Shul: J. Vac. Sci. Technol. B **17** (1999) 2015.
12) G. Hanington, Y. M. Hsin, Q. Z. Liu, P. M. Asbeck, S. S. Lau, M. Asif Khan, J. W. Yang, and Q. Chen: Electron. Lett. **34** (1998) 193.
13) M. Werquin, N. Vellas, Y. Guhel, D. Ducatteau, B. Boudart, J. C. Pesant, Z. Bougrioua, M. Germain, J. C. De Jaeger, and C. Gaquiere: Microwave Opt. Technol. Lett. **46** (2005) 311.
14) J. W. Johnson, E. L. Piner, A. Vescan, R. Therrien, P. Rajagopal, J. C. Roberts, J. D. Brown, S. Singhal, and K. J. Linthicum: IEEE Electron Device Lett. **25** (2004) 459.
15) J. Y. Shiu, J. C. Huang, V. Desmaris, C. T. Chang, C. Y. Lu, K. Kumakura, T. Makimoto, H. Zirath, N. Rorsman, and E. Y. Chang: IEEE Electron Device Lett. **28** (2007) 476.
16) S. O. Kucheyev, J. S. Williams, and S. J. Pearton: Mater. Sci. Eng. R **33** (2001) 51.
17) J. Kuzmík, P. Javorka, A. Alam, M. Marso, M. Heuken, and P. Kordoš: IEEE Trans. Electron Devices **49** (2002) 1496.
18) J.-Y. Shiu, V. Desmaris, N. Rorsman, K. Kumakura, T. Makimoto, H. Zirath, and E. Y. Chang: Semicond. Sci. Technol. **22** (2007) 717.
19) S. J. Pearton, M. P. Lannuzzi, C. L. Reynolds, and L. Peticolas: Appl. Phys. Lett. **52** (1988) 395.
20) S. M. Sze: J. Appl. Phys. **38** (1967) 2951.
21) V. Desmaris, M. Rudzinski, N. Rorsman, P. R. Larssen, H. Zirath, T. C. Rodle, and H. F. F. Jos: IEEE Trans. Electron Devices **53** (2006) 2413.
22) R. Chu, Y. Zhou, J. Liu, D. Wang, K. J. Chen, and K. M. Lau: IEEE Trans. Electron Devices **52** (2005) 438.